

Extrinsic Vector Field Processing

H. Liu¹  O. Stein²  A. Vaxman³  M. Ben-Chen²  M. Kazhdan¹ 

¹Johns Hopkins University, USA ²Technion, Israel ³University of Edinburgh, UK

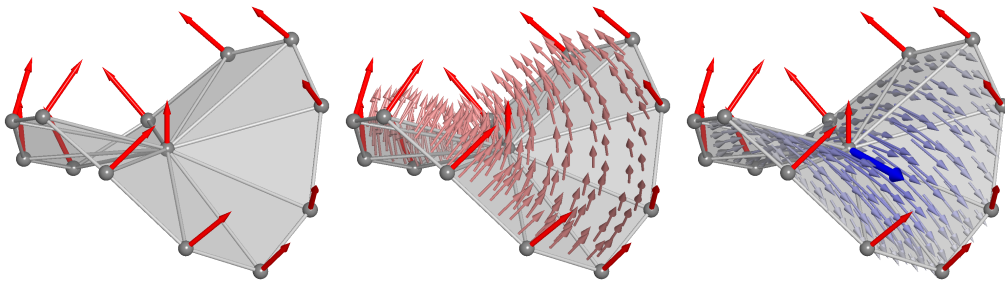


Figure 1: To define a continuous basis for tangent-vector fields over a triangle mesh, we start with a triangle mesh with per-vertex normals (left). Using Phong interpolation, we obtain a continuous normal field over the mesh (center). Then, given a tangent vector at a vertex (dark blue), we extend it into the interior of the incident triangles by (1) transporting the vertex's tangent using the Rodrigues rotation taking the vertex's normal to the interior point's normal, and (2) scaling the transported tangent by the vertex's barycentric coordinate.

Abstract

We propose a novel discretization of tangent vector fields for triangle meshes. Starting with a Phong map continuously assigning normals to all points on the mesh, we define an extrinsic bases for continuous tangent vector fields by using the Rodrigues rotation to transport tangent vectors assigned to vertices to tangent vectors in the interiors of the triangles. As our vector fields are continuous and weakly differentiable, we can use them to define a covariant derivative field that is evaluable almost-everywhere on the mesh. Decomposing the covariant derivative in terms of diagonal multiple of the identity, anti-symmetric, and trace-less symmetric components, we can define the standard operators used for vector field processing including the Hodge Laplacian energy, Connection Laplacian energy, and Killing energy. Additionally, the ability to perform point-wise evaluation of the covariant derivative also makes it possible for us to define the Lie bracket.

CCS Concepts

- Computing methodologies → Mesh models;
- Mathematics of computing → Quadrature; Differential calculus;

1. Introduction

Vector-field-processing is an essential step in a broad class of geometry-processing applications, supporting the study of deformations of signals over a mesh and has been a corner-stone in a large body of work including frame design, deformation, parallel transport, and optical flow. An essential first step in all these applications is defining a discretization of the vector-fields, enabling their representation, the study of their properties (e.g. smoothness), and the formulation of energies which have desired vector-fields as their minima.

A key challenge in discretizing vector fields, and in particular in

supporting the study of vector-field smoothness, is that the “natural” definition of vector fields would represent them by values associated with faces, where a tangent space can be defined as the space perpendicular to the face normal. However, such representations are inherently discontinuous, due to the piecewise-constant triangle normals, resulting in unbounded derivatives across edges and making smoothness energies challenging to define.

These challenges have typically been addressed in one of two ways: Discrete Exterior Calculus (DEC) techniques have been used to define discretizations of vector-fields and associated smoothness energies *without* explicitly constructing a basis. They provide a way

to optimize vector fields but only support evaluation at specific locations and in specific directions. The second approach is to use a discontinuous vector-field basis (e.g. Nédélec/Whitney, Raviart-Thomas, or Crouzeix-Raviart). These support point-wise evaluation and differentiation, but the discontinuity along edges means that only some differential operators are well-formulated in this representation.

An exception to this is the vector-field representation proposed by Knöppel *et al.* [KCPS13]. There, the authors propose extending an intrinsically represented tangent vector defined at a vertex into the incident triangles by a combination of parallel transport and linear scaling.

In our work we follow the approach of Knöppel *et al.*, replacing the intrinsic representation of tangent vectors with an explicit one, visualized in Figure 1. To this end we assume we are given a triangle mesh with per-vertex normals as input (left), which we extend to a continuous normal field over the mesh (center). Then, given a tangent vector at a vertex, we extend that vector to a continuous vector field over the mesh (right). Concretely, given a point in the interior of the incident triangle we define the tangent vector at that point by (1) using the Rodrigues rotation (taking the vertex's normal to the point's normal) to transport the tangent from the vertex to the point, and (2) scaling the transported tangent by the component of the point's barycentric coordinate associated with the vertex.

In addition to providing an extrinsic realization of Knöppel *et al.*'s discretization that is consistent with per-vertex normals, our approach provides a simple expression for the vector-field basis that supports point-wise differentiation. This, in turn, make it possible to define a covariant derivative this is point-wise evaluable, enabling the construction of mass, stiffness (Hodge and Connection), and Killing energies. It is also supports the point-wise evaluation of the Lie bracket of two vector fields.

To enable down-stream research we provide an implementation in C++, using a functional-programming paradigm, that makes it straight-forward to represent fields (tangent vector, and higher-order tensor) over the mesh. The implementation only requires that a user provide a functor evaluable at arbitrary positions on the mesh (defined by the triangle index and barycentric coordinates) and returns the field's value at that point. (These fields can themselves be constructed by evaluating vector-fields and their covariant derivatives to construct the field's values.) Using quadrature, the implementation integrates the fields, performing the finite-element assembly required to construct system matrices and vectors for targeted vector-field-processing applications.

2. Related Work

The goal of this work is to define an extrinsic connection Laplacian for triangle meshes embedded in \mathbb{R}^3 . As in the seminal work of Knöppel *et al.* [KCPS13] our approach is to define a finite-dimensional space of continuous vector-fields over the triangle mesh. However, unlike Knöppel *et al.*, we define the space of functions *extrinsically*, representing tangent vector-fields as functions, parameterized over points on the triangle mesh, taking values in \mathbb{R}^3 . For the vector-fields to be continuous we leverage the Phong representation of Boubekeur *et al.* [BA08], first defining a continuous

normal field over the surface, and then defining a space of tangent vector-fields that is everywhere orthogonal to the normals.

2.1. Properties

2.1.1. Discrete Exterior Calculus

In contrast to traditional methods which discretize zero-forms at vertices and one-forms along edges, and then define the associated differential, co-differential, and Hodge star operators, our approach uses a finite-elements formulation, in which basis functions are defined and operators are constructed by integrating products of functions and derivatives over the mesh.

While DEC-based approaches have the advantage of being mimetic, preserving certain symmetries/invariants at *any* discretization they have the disadvantage that they do not support function evaluation at arbitrary locations and along arbitrary directions on the mesh. An example is the computation of geodesic distances using the Heat Method [CWW17], which requires representing the *normalized* differential of a scalar function. This is not straightforward to do in the DEC framework as the edge-based representation only describes the evaluation of the differential along a particular direction (the direction of the edge), making it challenging to measure the differential's magnitude.

2.1.2. Whitney Basis

The standard DEC formulation can be realized in the finite-elements framework using the Whitney basis functions [DKT06], combining the mimetic properties of DEC with the point-wise evaluation of FEM. This resolves the above-mentioned challenge of computing geodesics, since the algorithm only requires that the normalized differential be integrated against the one-form basis functions, not that the normalized differential be expressible in the basis.

2.1.3. Complex Tangent Basis

Our approach can be thought of as an extrinsic analogue of the intrinsic basis presented by Knöppel *et al.* As such, we forego some of the advantages of the Whitney basis while gaining others. For example, the basis no longer has the property that the gradient of a function in the span of the scalar basis can be expressed as a linear combination of tangent basis functions. However, for oriented manifolds, the subspace of vector-fields is closed under rotation by 90° , and (as we will show) provides a discretization of the Lie bracket.

3. Background

To define the covariant derivative and decompose it into its constituent parts, we leverage some basic linear algebra, which we briefly review here. We also recall the expression for the (minimal) Rodrigues rotation and introduce notation that we will use throughout the remainder of the discussion (Table 1).

We note that as our approach is based on defining a basis for function spaces on a mesh, composed of functions that are defined “piecewise” per triangle, our discussion will focus on a single embedded triangle. Standard finite element assembly is then used to combine the per-triangle quantities into global system matrices/vectors.

3.1. Linear Algebra Review

In this work, we will be considering finite-dimensional inner-product spaces $\{V, B_V : V \rightarrow V^*\}$ with V the vector-space, V^* its dual, and B_V the symmetric, positive-definite, bilinear form defining the inner-product. (For simplicity, we will represent bilinear forms as linear maps from the primal space to the dual, so that operations like inversion are well-defined.)

Inner-Products on Linear Maps

Given inner-product spaces $\{V, B_V\}$ and $\{W, B_W\}$, there is a canonical inner-product on the space of linear maps between V and W , defined in terms of the trace:

$$B_{\text{Hom}(V,W)}(L, M) \equiv \text{tr} \left(B_V^{-1} \circ L^* \circ B_W \circ M \right) \quad (1)$$

with $L^* : W^* \rightarrow V^*$ the dual map. This definition is independent of the choice of bases for V and W . And, when expressed with respect to orthogonal bases for V and W , is equivalent to the Frobenius inner-product of the associated matrices. (We note that the argument to the trace is itself an endomorphism on V : M maps V to W , B_W maps W to W^* , L^* maps W^* to V^* , and B_V^{-1} maps V^* back to V . Thus, the trace is well-defined.)

Endomorphism Decomposition

We briefly summarize coordinate-free decomposition of the space of endomorphisms on an inner-product space $\{V, B_V\}$. For a more detailed discussion of factorization of the space of 2-tensors, we refer the reader to the work of de Goes *et al.* [dGLB¹⁴].

An endomorphism $L : V \rightarrow V$ is said to be *symmetric* if the bilinear form $B_V \circ L : V \rightarrow V^*$ is symmetric:

$$[(B_V \circ L)(v)](w) = [(B_V \circ L(w))](v), \quad \forall v, w \in V.$$

Analogously, an endomorphism $L : V \rightarrow V$ is *anti-symmetric* if:

$$[(B_V \circ L)(v)](w) = -[(B_V \circ L(w))](v), \quad \forall v, w \in V.$$

The subsets of symmetric/anti-symmetric endomorphisms form linear subspaces and we denote them as $\mathcal{S}ym(V)$ and $\mathcal{A}Sym(V)$ respectively. Given an endomorphism $L : V \rightarrow V$, the orthogonal projections onto $\mathcal{S}ym(V)$ and $\mathcal{A}Sym(V)$ are, respectively:

$$L \mapsto \left(\frac{L + B_V^{-1} \circ L^* \circ B_V}{2} \right) \quad \text{and} \quad L \mapsto \left(\frac{L - B_V^{-1} \circ L^* \circ B_V}{2} \right).$$

The space $\mathcal{S}ym(V)$ can be further decomposed into endomorphisms that are scalar multiples of the identity, $\mathcal{T}race(V)$ and endomorphisms with vanishing trace, $\overline{\mathcal{T}race}(V)$. Given a symmetric endomorphism $L \in \mathcal{S}ym(V)$, the orthogonal projections onto the subspaces are, respectively:

$$L \rightarrow \frac{\text{tr}(L)}{\dim(V)} \cdot \text{Id.} \quad \text{and} \quad L \rightarrow L - \frac{\text{tr}(L)}{\dim(V)} \cdot \text{Id.}$$

Thus, the partition of the space of endomorphisms:

$$\text{End}(V) = \mathcal{T}race(V) \oplus \overline{\mathcal{T}race}(V) \oplus \mathcal{A}Sym(V)$$

is an orthogonal decomposition of $\text{End}(V)$ with respect to the metric induced by B_V .

$R : S^2 \times S^2 \rightarrow \text{SO}(3)$	Rodrigues rotation
$v_i \in \mathbb{R}^3$	Vertices of the triangle
$n_i \in S^2$	Normals of the triangle
$n \in S^2$	Normal defined by triangle $\{v_0, v_1, v_2\}$
$\mathbb{T} \subset \mathbb{R}^2$	Unit right triangle
$S^2 \subset \mathbb{R}^3$	Unit sphere
$T_p \mathbb{T} \simeq \mathbb{R}^2$	Tangent space at $p \in \mathbb{T}$
$T_n S^2 \subset \mathbb{R}^3$	Tangent space at $n \in S^2$
$\text{End}(T_p \mathbb{T})$	The space of endomorphisms on $T_p \mathbb{T}$
$\Phi : \mathbb{T} \rightarrow \mathbb{R}^3$	Linear embedding of triangle $\{v_0, v_1, v_2\}$
$d\Phi _p : T_p \mathbb{T} \rightarrow T_n S^2$	Differential of Φ at $p \in \mathbb{T}$
$g _p : T_p \mathbb{T} \rightarrow T_p \mathbb{T}^*$	Metric on $T_p \mathbb{T}$ induced by $d\Phi _p$
$N : \mathbb{T} \rightarrow S^2$	Gauss map defined by vertex normals
$\widetilde{d\Phi} _p : T_p \mathbb{T} \rightarrow T_{N(p)} S^2$	Realization of $T_p \mathbb{T}$ in $T_{N(p)} S^2$
$\psi_i : \mathbb{T} \rightarrow \mathbb{R}$	Hat basis
$\mathbf{m}^\psi \in \mathbb{R}^{3 \times 3}$	Element scalar mass matrix
$\mathbf{s}^\psi \in \mathbb{R}^{3 \times 3}$	Element scalar stiffness matrix
$R_i : \mathbb{T} \rightarrow \text{SO}(3)$	Parallel transport from the i -th corner
$\overline{\omega}_i : \mathbb{T} \rightarrow \mathbb{R}^3$	Extrinsic tangent vector field basis
$\omega_i \in \Gamma(T\mathbb{T})$	Pulled-back tangent vector field basis
$\mathcal{V} \subset \mathbb{R}^3$	Mesh vertices
$\mathcal{T} \subset [0, \mathcal{V}]^3$	Mesh triangles
$\mathbf{M}^\psi \in \mathbb{R}^{ \mathcal{V} \times \mathcal{V} }$	Mesh scalar mass matrix
$\mathbf{S}^\psi \in \mathbb{R}^{2 \mathcal{V} \times 2 \mathcal{V} }$	Mesh scalar stiffness matrix

Table 1: Notation for per-triangle system construction

3.2. Rodrigues Rotation

Given (non-antipodal) unit vectors $v, w \in S^{d-1}$, the Rodrigues rotation formula gives the minimal-angle rotation taking v to w :

$$R(v, w) \equiv \text{Id.} + (w \cdot v^\top - v \cdot w^\top) + \frac{(w \cdot v^\top - v \cdot w^\top)^2}{1 + \langle v, w \rangle} \in \text{SO}(d).$$

We note that this expression is singular only when v and w are antipodal, in which case the rotation by 180° in any plane containing v will be minimal.) Otherwise, the coefficients of R are smooth functions of v and w , with derivatives that are readily computable.

3.3. Notation

Given a triangle with vertices $v_0, v_1, v_2 \in \mathbb{R}^3$, we denote the triangle's normal as:

$$n = \frac{(v_1 - v_0) \times (v_2 - v_0)}{\|(v_1 - v_0) \times (v_2 - v_0)\|}.$$

Computations are performed over the unit right triangle and unit sphere, $\mathbb{T} \subset \mathbb{R}^2$ and $S^2 \subset \mathbb{R}^3$:

$$\mathbb{T} = \{(s, t) \in [0, 1]^2 \mid s + t \leq 1\} \quad \text{and} \quad S^2 = \{n \in \mathbb{R}^3 \mid |n| = 1\}.$$

The tangent space at $p \in \mathbb{T}$ is equivalent to Euclidean 2-space and the tangent space at $n \in S^2$ is a subset of Euclidean 3-space:

$$T_p \mathbb{T} \simeq \mathbb{R}^2 \quad \text{and} \quad T_n S^2 \subset \mathbb{R}^3.$$

We denote by $\Phi : \mathbb{T} \rightarrow \mathbb{R}^3$ the linear embedding of the triangle:

$$\Phi(s, t) = (1 - s - t) \cdot v_0 + s \cdot v_1 + t \cdot v_2$$

and we set $d\Phi|_p$ to be its differential at $p \in \mathbb{T}$:

$$d\Phi|_p : T_p \mathbb{T} \simeq \mathbb{R}^2 \rightarrow T_n S^2 \subset \mathbb{R}^3.$$

We set $g|_p$ to be the metric tensor on $T_p\mathbb{T}$ induced by the linear embedding of the unit right triangle:

$$g|_p = d\Phi|_p^\top \cdot d\Phi|_p.$$

We assume that we are given a Gauss Map:

$$N : \mathbb{T} \rightarrow S^2.$$

We denote by $\widetilde{d\Phi}|_p$ the map “realizing” the tangent space $T_p\mathbb{T}$ as a subspace of \mathbb{R}^3 perpendicular to $N(p)$ by first computing the differential of the embedding Φ and then applying the Rodrigues rotation taking the normal of the embedded triangle to the normal prescribed by the Gauss Map.

$$\widetilde{d\Phi}|_p \equiv R(n, N(p)) \circ d\Phi|_p : \mathbb{R}^2 \rightarrow \mathbb{R}^3.$$

We denote the “hat” functions as $\psi_i : \mathbb{T} \rightarrow \mathbb{R}$, with:

$$\phi_0(s, t) = 1 - s - t, \quad \phi_1(s, t) = s, \quad \text{and} \quad \phi_2(s, t) = t,$$

We note that: (1) The differential $d\Phi|_p$, and hence the metric $g|_p$ is constant for all $p \in \mathbb{T}$; (2) The realization $\widetilde{d\Phi}|_p$ is an orthogonal transformation between $T_p\mathbb{T}$ with inner-product $g|_p$ and $T_{N(p)}S^2$ with inner-product obtained by restricting the Euclidean inner-product on \mathbb{R}^3 ; (3) The inverse of $\widetilde{d\Phi}|_p$ is:

$$\widetilde{d\Phi}|_p^{-1} \equiv g^{-1} \cdot d\Phi|_p^\top \cdot R(N(p), n) \quad (2)$$

and is defined over all of \mathbb{R}^3 by projecting out the component parallel to $N(p)$.

4. Discretization

To describe our implementation, it suffices to consider the case of a single triangle, as the global system can then be constructed using finite-element assembly. To this end, we assume that we are given a triplet of oriented vertices $\{v_i, n_i\} \in \mathbb{R}^3 \times S^2$, and we extend the per-vertex normals to a Gauss map $N : \mathbb{T} \rightarrow S^2$ by interpolation and normalization:

$$N(p) \equiv \frac{\sum_i \psi_i(p) \cdot n_i}{|\sum_i \psi_i(p) \cdot n_i|} \in S^2.$$

4.1. Scalar Basis

Using the standard “hat” functions gives the mass, $\mathbf{m}^\psi \in \mathbb{R}^{3 \times 3}$, and stiffness, $\mathbf{s}^\psi \in \mathbb{R}^{3 \times 3}$, matrices:

$$\begin{aligned} \mathbf{m}_{ij}^\psi &\equiv \int_{\mathbb{T}} \psi_i(p) \cdot \psi_j(p) \cdot \sqrt{\det(g|_p)} \, dp \\ \mathbf{s}_{ij}^\psi &\equiv \int_{\mathbb{T}} \text{tr} \left(g|_p^{-1} \cdot d\psi_i|_p^\top \cdot d\psi_j|_p \right) \cdot \sqrt{\det(g|_p)} \, dp. \end{aligned}$$

(The definition of the stiffness matrix is consistent with Equation 1, implicitly using the fact that the inner-product on \mathbb{R}^3 , expressed in terms of the coordinate basis, is the identity.)

4.2. Vector-Field Basis

To define a basis for vector-fields, we proceed as in the approach of Knöppel *et al.*, (1) defining a parallel transport operator taking tangent vectors at the vertices to tangent vectors in the interior of a

triangle, (2) selecting a tangent frame at each vertex, and (3) blending the transported tangent vectors. As we do this extrinsically, we begin by defining an interpolated normal field in the standard way.

Parallel transport Given a tangent vector $t_i \in \mathbb{R}^3$ at the i -th corner (perpendicular to n_i), we define its parallel transport to $p \in \mathbb{T}$ by applying the Rodrigues rotation taking n_i to $N(p)$, to the tangent vector t_i . We denote by $R_i : \mathbb{T} \rightarrow \text{SO}(3)$ the minimal-angle rotation taking the normal at the i -th corner to the interpolated normal at p :

$$R_i(p) \equiv R(n_i, N(p)).$$

Framing Vertices At the i -th corner we select tangent vectors, $t_{2i}, t_{2i+1} \in \mathbb{R}^3$ perpendicular to the normal n_i . For simplicity, we choose the vectors to be unit-norm and orthogonal. (As in Knöppel *et al.*, the choice of per-corner frame does not change the function space.)

Blending Transported Tangent Vectors We extend the tangent vectors, $t_i \in \mathbb{R}^3$, to vector-fields defined in the interior of the triangle, $\bar{\omega}_i : \mathbb{T} \rightarrow \mathbb{R}^3$, using parallel transport and blending:

$$\bar{\omega}_{2i+k}(p) \equiv \psi_i(p) \cdot R_i(p) \cdot t_{2i+k} \quad \text{with } k \in \{0, 1\} \quad (3)$$

We note that, by construction, these are perpendicular to the interpolated normals. Differentiating Equation (3) we get a field giving the change in the 3D vector-field as a function of tangent direction:

$$d\bar{\omega}_j|_p : T_p\mathbb{T} \rightarrow \mathbb{R}^3.$$

We pull these back to get vector fields on the tangent space of the unit right triangle, and their associated covariant derivatives:

$$\omega_i|_p \equiv \widetilde{d\Phi}|_p^{-1} \cdot \bar{\omega}_i|_p \in T_p\mathbb{T}$$

$$\nabla \omega_i|_p \equiv \widetilde{d\Phi}|_p^{-1} \circ d\bar{\omega}_i|_p \in \text{End}(T_p\mathbb{T}).$$

We recall that as $\widetilde{d\Phi}|_p^{-1}$ projects out the normal component, the covariant derivative is only defined in terms of the component of $d\bar{\omega}_i$ in the tangent space $T_{N(p)}S^2$.

Using the six functions $\omega_i : \mathbb{T} \rightarrow \mathbb{R}^3$ we compute the mass and stiffness matrices, $\mathbf{m}^\omega, \mathbf{s}^\omega \in \mathbb{R}^{6 \times 6}$ with:

$$\begin{aligned} \mathbf{m}_{ij}^\omega &\equiv \int_{\mathbb{T}} \langle \bar{\omega}_i|_p, \bar{\omega}_j|_p \rangle \cdot \sqrt{\det(g|_p)} \, dp \\ \mathbf{s}_{ij}^\omega &\equiv \int_{\mathbb{T}} \text{tr} \left(g|_p^{-1} \cdot (\nabla \omega_i|_p)^\top \cdot g|_p \cdot (\nabla \omega_j|_p) \right) \cdot \sqrt{\det(g|_p)} \, dp. \end{aligned} \quad (4)$$

4.3. Integration

For both the scalar and vector-field basis we compute the coefficients of the mass and stiffness matrices using numeric quadrature [Tay08]. For the mass matrices, this only requires that we can evaluate the basis functions at arbitrary locations in the triangle. For the stiffness matrix, this also requires that we are able to evaluate the differential of the basis functions. This is trivial for the scalar basis (since the differential is constant) and, given the simple expression of the Rodrigues rotation formula, can and also be implemented for the vector field basis.

Though the use of quadrature for computing integrals can result in numerical error (e.g. when the integrated function is not a

polynomial of an appropriately low degree), it has the advantage of allowing the definition of linear systems in which the right-hand-side (constraints) is not in the span of the function basis. This is the case for computing geodesics discussed above, and is also true more generally when the signal is not defined by interpolating values from the vertices, such as when using texture maps or neural implicits [PFS*19].

4.4. Finite Element Assembly

Given a triangle mesh, $\{\mathcal{V}, \mathcal{T}\}$, and given functionality for computing the system matrix associated to a triangle, $M : \mathcal{T} \rightarrow \mathbb{R}^{3K \times 3K}$, pseudocode for finite element assembly is summarized in Algorithm 1: The matrix is initialized (Step 1), iterating over all triangles (Step 2), the system matrix for the triangle is computed (Step 3), and its coefficients are added to the corresponding entries of the system matrix defined over the mesh (Steps 4-7).

Algorithm 1: FiniteElementAssembly

Require: $L : \mathcal{T} \rightarrow \mathbb{R}^{3K \times 3K}$

```

1:  $\mathbf{L} \leftarrow \mathbf{0} \in \mathbb{R}^{|\mathcal{V}|K \times |\mathcal{V}|K}$ 
2: for  $\tau = \{v_0, v_1, v_2\} \in \mathcal{T}$ :
3:    $\mathbf{l} \leftarrow L(\tau)$ 
4:   for  $m, n \in [0, 3)$  and  $k, l \in [0, K)$ :
5:      $I \leftarrow v_m \cdot K + k, \quad J \leftarrow v_n \cdot K + l$ 
6:      $i \leftarrow m \cdot K + k, \quad j \leftarrow n \cdot K + l$ 
7:      $\mathbf{L}_{IJ} \leftarrow \mathbf{L}_{IJ} + \mathbf{l}_{ij}$ 
8: return  $\mathbf{L}$ 
```

For the scalar mass and stiffness matrices, which have one degree of freedom per vertex, we have $K = 1$. For the vector-field mass and stiffness matrices we have $K = 2$. In what follows, we abuse notation, using ψ_i (resp. ω_{2i} and ω_{2i+1}), with $i \in [0, |\mathcal{V}|]$, to denote the scalar (resp. vector-field) basis functions on the mesh, rather than at the corners of a single triangle.

5. Energies and Operators

While the previous section described the construction of the stiffness matrix for vector-fields, corresponding to the Dirichlet energy defined by the covariant derivative, a similar approach can be used to define other energies. We also show that our discretization can be used to define the Lie bracket operator.

We note that the subsequent discussion holds for all finite-elements discretization of vector fields that supports differentiation. In particular, we discuss constructions of the Killing energy and definitions of the Lie bracket derived from the finite-elements proposed by Stein *et al.* [SWJG20]. While in principal a similar approach can be used with the finite-elements of Knöppel *et al.* [KCPS13], the lack of a closed-form expression for the basis functions makes this challenging in practice.

5.1. Energies

Using the decomposition from Section 3.1, we can factor the covariant derivative into orthogonal components consisting of scalar

multiples of the identity, trace-free (symmetric) endomorphisms, and anti-symmetric endomorphisms. This, in turn, allows us to replace the covariant derivative in Equation 4 with an individual component – allowing us to define classical energies used in vector-field processing such as:

$$\begin{aligned} \text{Connection} &\longleftrightarrow \text{Trace}(T_p \mathbb{T}) \oplus \overline{\text{Trace}}(T_p \mathbb{T}) \oplus \mathcal{ASym}(T_p \mathbb{T}) \\ \text{Holom. / Hodge} &\longleftrightarrow \text{Trace}(T_p \mathbb{T}) \oplus \mathcal{ASym}(T_p \mathbb{T}) \\ \text{Anti-holom.} &\longleftrightarrow \overline{\text{Trace}}(T_p \mathbb{T}) \\ \text{Killing} &\longleftrightarrow \text{Trace}(T_p \mathbb{T}) \oplus \overline{\text{Trace}}(T_p \mathbb{T}) \\ \text{Divergence} &\longleftrightarrow \text{Trace}(T_p \mathbb{T}) \\ \text{Curl} &\longleftrightarrow \mathcal{ASym}(T_p \mathbb{T}) \end{aligned}$$

5.2. Lie Bracket

Our approach provides an expression for the covariant derivative that can be evaluated pointwise. In addition to being amenable to quadrature-based integration, making it easy to define the energies described above, it also enables the pointwise evaluation of the Lie bracket of two vector fields.

Concretely, given tangent vector-fields X and Y , we evaluate the Lie bracket at a point $p \in \mathbb{T}$ by taking the difference of the derivative of X at p along direction $Y(p)$ and the derivative of Y at p along direction $X(p)$:

$$[X, Y](p) = \nabla X|_p \cdot Y(p) - \nabla Y|_p \cdot X(p).$$

Global fitting

As our space of tangent vector-fields is not closed under the Lie bracket, it is generally not the case that the bracket of vector fields X and Y can be expressed as a linear combination of our tangent vector-field basis. However, it is straightforward to compute the projection of the bracket $[X, Y]$ onto our space of vector-fields.

Given tangent vector-fields X and Y , we start by computing the “weak representation” of their Lie bracket, $\mathbf{b} \in \mathbb{R}^{2|\mathcal{V}|}$, by computing the integral of dot-product of the bracket with the tangent vector-field basis functions:

$$\mathbf{b}_i \equiv \int \text{tr} \left(\omega_i^\top(p) \cdot g|_p \cdot [X, Y](p) \right) \cdot \sqrt{\det(g|_p)} \, dp.$$

Then, we obtain the coefficients of the projection of the bracket onto the space of tangent vector-fields, $\mathbf{z} \in \mathbb{R}^{2|\mathcal{V}|}$, by solving:

$$\mathbf{M}^\omega \cdot \mathbf{z} = \mathbf{b}. \quad (5)$$

6. Evaluation

We evaluate our discretization of the space of tangent vector-fields in three ways: We validate that it preserves some basic invariants from the continuous theory; We compare to existing discretizations, focusing in particular on the work of Knöppel *et al.* [KCPS13], Sharp *et al.* [SSC19], and Stein *et al.* [SWJG20]; We demonstrate applications of our approach in computing the Lie bracket of vector fields.

For all our evaluations, we use 3-point quadrature to integrate

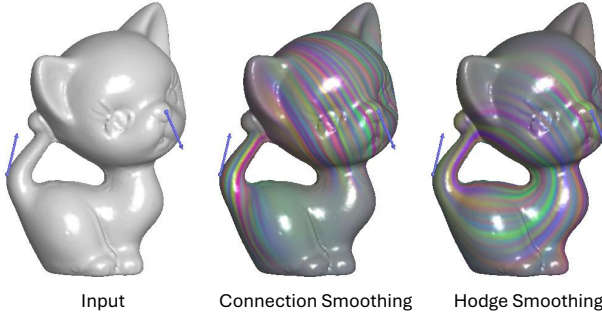


Figure 2: Visualization of smooth interpolation of sparse vectors (draw in blue) using a Dirichlet energy defined by the Connection (center) and Hodge (right) Laplacians.

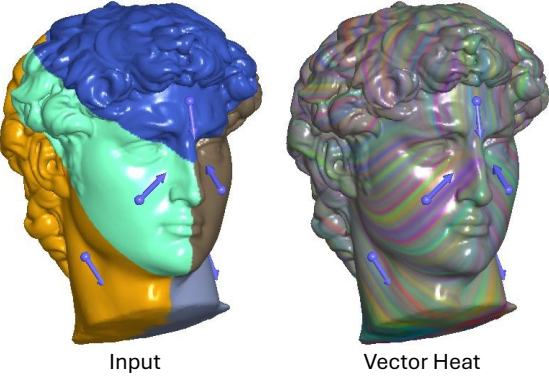


Figure 3: Input point constraints, with associated Voronoi partition of the geometry (left) and the result of applying the Vector Heat method (right).

functions over a triangle. With the exception of the unit sphere we rescale all models to have unit area. We assign normals to vertices by computing the approximate limit surface under Loop subdivision [Loo87]. Concretely, for each vertex we compute the subdivision stencil, raised to the 10-th power, and apply it to the vertex and its one-ring neighbors. We then set the vertex's normal to the area-weighted average of the normals of the subdivided triangles. And, when ground-truth is available, we measure the error between the estimated solution, x and the ground-truth, x^* as the ratio:

$$E(x, x^*) \equiv \sqrt{\frac{\|x - x^*\|^2}{\|x\|^2 + \|x^*\|^2}}$$

where, for a function/field f defined on the surface, the notation $\|f\|^2$ denotes the integrated square-norm, over the mesh.

We begin with by considering several applications from geometry processing before proceeding to an empirical evaluation.

6.1. Example Applications

Sparse Vector Field Interpolation

Given a sparse subset of vertices $\mathcal{W} \subset \mathcal{V}$, and given target tangent vectors at those vertices $\{\mathbf{t}_w\}_{w \in \mathcal{W}}$, the stiffness matrix can be used to solve for the as-smooth-as-possible interpolating vector-field:

$$\mathbf{x} = \underset{\mathbf{y} \in \mathbb{R}^{3|\mathcal{V}|}}{\operatorname{argmin}} \left(\mathbf{y}^\top \cdot \mathbf{S} \cdot \mathbf{y} \right), \quad \text{s.t.} \quad \mathbf{y}_w = \mathbf{t}_w, \forall w \in \mathcal{W}$$

with \mathbf{S} a stiffness matrix.

As an example, Figure 2 shows a model with two tangent vector constraints (blue) and the computed vector-fields obtained with \mathbf{S} defined by the connection (center) and Hodge (right) energies. As the model has genus one, there are two harmonic vector fields and Hodge smoothing gives the vector-field circulating around the hole. In contrast, the connection energy, which is non-singular, penalizes the vector-field wherever it is non-zero, resulting in an interpolant that gets smaller away from the constraints.

Vector Heat

As another application, we consider the Vector Heat method for performing parallel transport of vectors [SSC19]. The method is

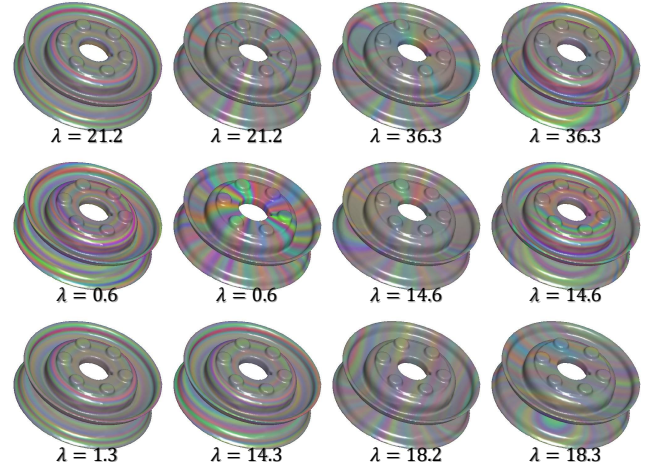


Figure 4: Visualization of The four smallest eigenvectors of the Connection (top), Hodge (middle), and Killing (bottom) energies.

implemented by performing one step of vector heat diffusion (using the connection Laplacian) as well as two steps of scalar heat diffusion (using the co-tangent Laplacian). Combining these, one obtains a vector field on the surface whose value within a Voronoi region of a constraint point is the parallel transport of the constraint vector along the shortest path geodesic.

Figure 3 shows the results for five constraint vectors placed on the surface of the David model. The visualization shows the initial constraint vectors and associated Voronoi regions (left) as well as the output vector field (right).

Spectral Fields

Using the energies from Section 5.1, we solve the generalized eigenproblem $\mathbf{S} \cdot \mathbf{x} = \lambda \mathbf{M} \cdot \mathbf{x}$ where \mathbf{M} is the mass matrix and \mathbf{S} is one of the connection, Hodge, and Killing energies.

Figure 4 visualizes the smallest four eigenvectors of each en-

ergy, along with the associated eigenvalues. We make several observations about the results:

- Since the connection and Hodge energies use equal weights of $\text{Trace}(T_p\mathbb{T})$ and $\mathcal{ASym}(T_p\mathbb{T})$, their eigenvectors comes in pairs, related by 90° -rotation (see discussion about in-plane rotation in § 6.2).
- Since the model has genus one, the two smallest eigenvectors of the Hodge Laplacian closely match the harmonic vector fields and their associated eigenvalues are close to zero.
- Because the pulley is nearly a surface of revolution, the smallest eigenvector of the Killing energy corresponds to the flow around the axis of revolution, and its associated eigenvalue is noticeably smaller than the next smallest eigenvalue. (Note that the the second eigenvector also corresponds to a vector-field circulating about the axis of rotational symmetry. However, the directions of flow are reversed on the top and bottom halves of the pulley.)

For visualization, we further decompose the eigenspaces of the connection and Hodge energies. To this end, we set $\mathbf{M} \in \mathbb{R}^{2|\mathcal{V}| \times 2|\mathcal{V}|}$ to be the mass matrix and $\mathbf{T} \in \mathbb{R}^{2|\mathcal{V}| \times 2|\mathcal{V}|}$ to be the stiffness matrix associated with component $\text{Trace}(T_p\mathbb{T})$ — the quadratic energy giving the integrated squared divergence of a vector-field. Then, for a particular eigenspace, X , of dimension $2k$, letting $\mathbf{X}^{|\mathcal{V}| \times 2k}$ be the matrix whose columns are the eigenvectors, we define matrices $\mathbf{m}, \mathbf{t} \in \mathbb{R}^{2k \times 2k}$ with:

$$\mathbf{m} = \mathbf{X}^\top \cdot \mathbf{M} \cdot \mathbf{X} \quad \text{and} \quad \mathbf{t} = \mathbf{X}^\top \cdot \mathbf{T} \cdot \mathbf{X}.$$

Solving the generalized eigenvalue problem:

$$\mathbf{t} \cdot \mathbf{x} = \lambda \mathbf{m} \cdot \mathbf{x}$$

we obtain an orthogonal basis for the eigenspace X graded by divergence energy. In particular, letting $\mathbf{x}_1, \dots, \mathbf{x}_{2k}$ be the computed eigenvectors, we order the eigenvectors as k pairs, with the first vector divergence-free and the second its 90° rotation:

$$\{\mathbf{X} \cdot \mathbf{x}_1, \mathbf{J} \cdot \mathbf{X} \cdot \mathbf{x}_1, \dots, \mathbf{X} \cdot \mathbf{x}_k, \mathbf{J} \cdot \mathbf{X} \cdot \mathbf{x}_k\}.$$

Comparison to Stein et al.

In principle, the finite-elements formulation of Stein *et al.* [SWJG20] can also be used to define a Killing energy. However, as discussed in that work, the direct definition of such an energy exhibits spurious high-frequency minima (likely due to aliasing arising from the discontinuous nature of the basis). This limitation was mitigated by introducing an additional (connection) smoothness regularizer to the Killing energy, though that introduces the additional challenge of tuning the regularization weight. Please see the appendix for additional discussion.

6.2. Quantitative Evaluation

Spectral Analysis on the Sphere

We consider the spectral decomposition of the connection Laplacian defined over the sphere. We generated ten random triangulations of the unit sphere in two ways: For the first, we randomly sampled points on the sphere and triangulated the points by computing the convex hull. For the second, we randomly sampled points on the ellipse with semi-axis lengths $(1, 4, 1)$, triangulated the points

by computing the convex hull, and rescaled the points to have unit-norm. We then computed the mass and connection Laplacian matrices, \mathbf{M} and \mathbf{S} and solved the generalized eigenvalue problem:

$$\mathbf{S} \cdot \mathbf{x} = \lambda \mathbf{M} \cdot \mathbf{x}$$

to obtain the first 240 eigenvalues.

As the n -th eigen-space of the connection Laplacian is $(4n+2)$ -dimensional, with associated eigenvalue $n(n+1)-1$, we evaluate the connection Laplacian by measuring the difference of the estimated eigenvalues from the ground-truth.

Figure 5 compares our results to those of Knöppel *et al.* [KCPS13], Stein *et al.* [SWJG20], and Sharp *et al.* [SSC19], with implementations provided by the authors ([SC*19, CS13]). For the visualization, we plot the ratio $|ev_c - ev_{gt}| / |ev_c + ev_{gt}|$, with ev_c the computed eigenvalue and ev_{gt} the ground-truth eigenvalue. Since the matrix of Sharp *et al.* is not obtained using a finite-elements approach, it is not guaranteed to be positive semi-definite when the mesh is not Delaunay, and we applied intrinsic Delaunay triangulation [FSBS06] before computing their Laplacian. For methods discretizing vector-fields using two values per vertex (ours, as well as those of Knöppel *et al.* and Sharp *et al.*) we sampled the sphere with $60K$ points. For the method of Stein *et al.*, which discretizes vector-fields using two values per edge, we sampled the sphere with $20K$ points. Consequently, all connection Laplacians were discretized by matrices of size (roughly) $120K \times 120K$.

For both the isotropically (top) and anisotropically (bottom) sampled sphere, our results are indistinguishable from those of Knöppel *et al.* and are comparable to those of the more recent method of Stein *et al.* While also comparable to the method of Sharp *et al.* for the anisotropically sampled sphere, we find that the spectrum of Sharp *et al.*'s Laplacian is closer to that of the ground-truth in the case of anisotropic sampling. We believe that this is due to the use of the intrinsic Delaunay triangulation.

Note In computing the spectrum using the methods of Sharp *et al.* and Stein *et al.*, we used the lumped (i.e. diagonal) mass matrix, whereas the unlumped matrix was used for Knöppel *et al.* and ours. As has been observed by others, we found that using the lumped matrix results in an under-estimate of the eigenvalues while using the unlumped matrix results in over-estimate (particularly for the isotropic sampling). This is visualized in Figure 5 by the tendency of the error of our discretization and that of Knöppel *et al.* to increase within eigenblock, while the error of Sharp *et al.* and Stein *et al.* tends to decrease. Replacing the unlumped matrix with the lumped matrix (which is reasonable under the assumption that the tangent space is framed using an orthonormal basis) similarly resulted in an under-estimate of the eigenvalues, but did not noticeably affect the magnitude of the errors.

Hodge Laplacian

Considering just the holomorphic component of the covariant derivative (i.e. the sum of the projections onto $\text{Trace}(T_p\mathbb{T})$ and $\mathcal{ASym}(T_p\mathbb{T})$) we obtain a quadratic energy on the space of vector-fields that is associated with the Hodge Laplacian.

We measure the similarity between the spectra of our holomor-

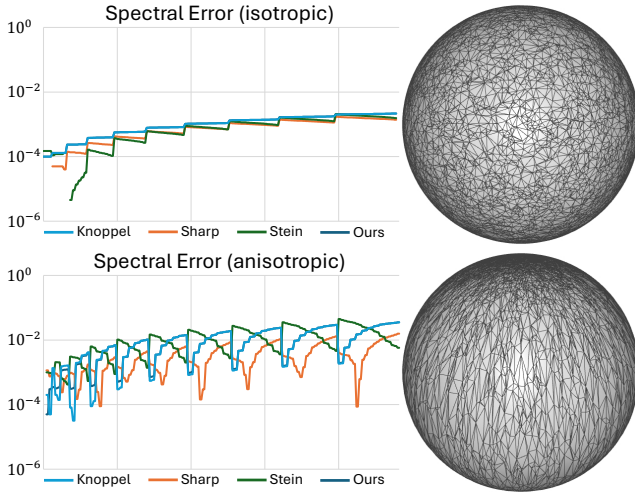


Figure 5: The differences between the analytic eigenvalues and the estimated ones, averaged over ten random tessellations of the unit sphere, as a function of eigenvalue index are shown on the right. The top chart plots results when the sphere was sampled isotropically. The bottom plots results for the more challenging case of anisotropic sampling. (The associated eigenvalues are $\{1, 5, 11, 19, 29, 41, 55, 71, 89, 109\}$.) Representative tessellations of the sphere, using 10K vertices for ease of visibility, are shown on the right.

phic energy and the spectra of the co-tangent Laplacian. We compare with the spectra obtained using the Hodge Laplacian computed using the Whitney basis. For both methods, we use the lumped mass matrix for 0-forms, since the definition of the Hodge energy using the DEC formulation requires inverting this matrix.

Figure 6 shows results for a number of shapes, with different genera. For both approaches we plot the ratio $|ev_h - ev_c|/|ev_h + ev_c|$ where ev_h is the eigenvalue of the Hodge Laplacian and ev_c is the associated eigenvalue of the co-tangent Laplacian, for the first 200 eigenvalues. Concretely, for a genus g surface, we compare eigenvalues $2(g+i)$ and $2(g+i)+1$ of the Hodge Laplacian with eigenvalue $i+1$ of the co-tangent Laplacian, accounting for the $2 \cdot g$ harmonic vector fields and constant scalar field.

In addition to comparing the spectra in general, the plots also give the ratio, ρ , of the $2g$ -th and $(2g+1)$ -st eigenvalues of our Hodge Laplacian. Since we expect to have $2g$ harmonic vector-fields, this ratio measures the extent to which the Hodge Laplacian fails to identify the harmonic vector-fields.

As the Whitney 1-forms are consistent with the mimetic DEC discretization, that approach always successfully identified the harmonics ($\rho = 0$). Furthermore, since the differentials of the eigenvectors of the co-tangent Laplacian are themselves eigenvectors of the Hodge Laplacian, every eigenvalue of the co-tangent Laplacian will necessarily be an eigenvalue of the Hodge Laplacian obtained using the DEC formulation. However, since the Whitney 1-forms are not closed under rotation by 90° degrees (see following discussion on in-plane rotation), the eigenvalues obtained using the DEC

discretization do not come in pairs and it is *not* the case that the $(i+1)$ -st eigenvalue of the co-tangent Laplacian will appear as either the $(2g+2i)$ -th or $(2g+2i+1)$ -st eigenvalue of the Hodge Laplacian discretized using DEC. Thus, while the DEC discretizations tends to give errors where every other one is initially zero, this ceases to hold for higher frequencies.

More generally, we found that at lower frequencies, the spectrum of the Whitney discretizations does a better job of matching the spectrum of the co-tangent Laplacian, while at higher frequencies our discretization does better.

To better understand the behavior of our discretizations under refinement, we repeated the experiment comparing the spectrum of the Hodge Laplacian to the spectrum of the co-tangent Laplacian, performing multiple passes of Loop subdivision [Loo87]. Figure 7 shows the results for the genus-3 elephant model. While we find that both our and the Whitney energies improve with refinement, and the extent of improvement appears to be consistent between the two methods. We also find that the trend of the Whitney basis outperforming our discretization at lower frequencies persists. Finally, though refinement improves the fit between the spectrum obtained using our discretization and the spectrum obtained using the co-tangent Laplacian, the ability of our discretization to distinguish the harmonic vector fields does not appear to improve consistently under refinement.

In-plane Rotation

As with the discretizations of Knöppel *et al.* and Stein *et al.*, our function space is closed under pointwise rotation by a fixed angle in the tangent plane. In particular, letting $\mathbf{M}, \mathbf{T}, \bar{\mathbf{T}}, \mathbf{A}, \mathbf{J} \in \mathbb{R}^{2|\mathcal{V}| \times 2|\mathcal{V}|}$ be the matrices corresponding to the:

- \mathbf{M} mass,
- \mathbf{T} stiffness of component $\text{Trace}(T_p \mathbb{T})$,
- $\bar{\mathbf{T}}$ stiffness of component $\overline{\text{Trace}}(T_p \mathbb{T})$,
- \mathbf{A} stiffness of component $\mathcal{A}\text{Sym}(T_p \mathbb{T})$, and
- \mathbf{J} 90° -rotation around each vertex's normal,

we validate that the mass matrix and trace-less component are both invariant under rotation by 90° and that the scalar-multiple of the identity and anti-symmetric components are related to each other by 90° -rotation.

For the models in Figure 6, we show the relative errors in Table 2. The table validates the expected properties of the system matrices under rotation by 90° . The tiny relative errors for the mass matrix are expected, given that the vector-field representation is extrinsic and that the Euclidean inner-product is invariant under rotation. For the other energies, the relative error is also small, with the largest errors for the “bunny” and “icosahedron” models. We believe this is due to the poor quality of the triangulations (both models were obtained by applying Marching-Cubes [LC87] to an implicit representation) which results in numerical precision issues. In particular, considering the distribution of triangle aspect ratios in Figure 8, we find that the error is strongly correlated with triangulation quality. (We note that as $\mathbf{J}^\top = -\mathbf{J}$ and $\mathbf{J}^\top \cdot \mathbf{J} = -\mathbf{Id}$, it follows that if $\mathbf{T} = \mathbf{J}^\top \cdot \mathbf{A} \cdot \mathbf{J}$ then $\mathbf{A} = \mathbf{J}^\top \cdot \mathbf{T} \cdot \mathbf{J}$ as well. This was empirically confirmed by noting that the relative errors are nearly identical.)

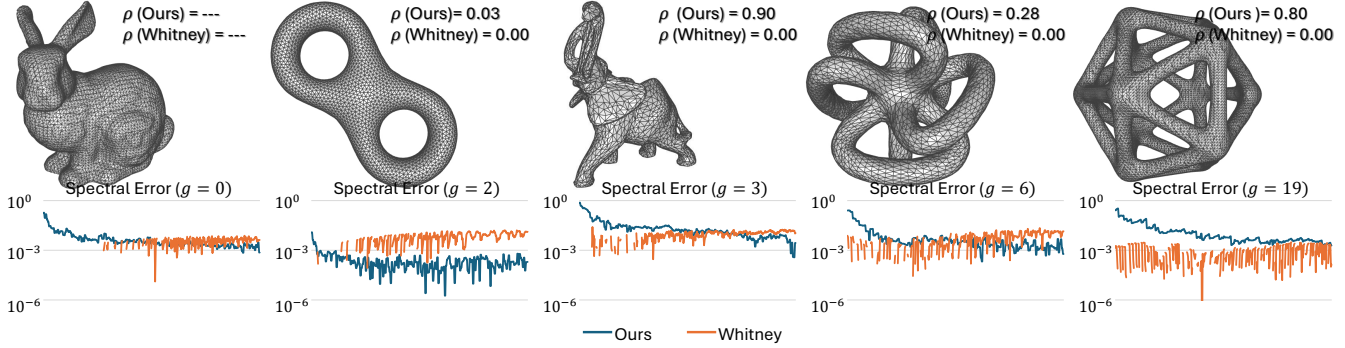


Figure 6: The relative difference between the eigenvalue of the Hodge Laplacian and the co-tangent Laplacian, computed using the holomorphic part of the connection Laplacian and the discretization using the Whitney basis. The plot also gives the genus, g , of the model and the ratio, ρ , of eigenvalues $2g$ and $2g + 1$.

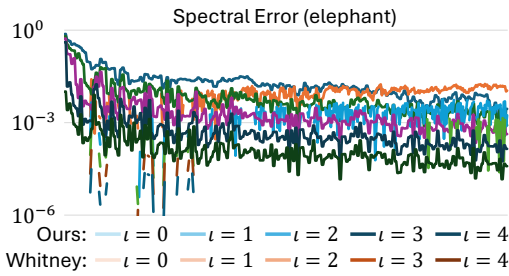


Figure 7: Comparison of relative eigenvalue differences computed for the “Elephant” model, with $i \in \{0, \dots, 4\}$ passes of Loop subdivision. For our discretization, the ratios of eigenvalues $2g$ and $2g + 1$ are, respectively, $\{0.89, 0.69, 0.85, 0.45, 0.70\}$.

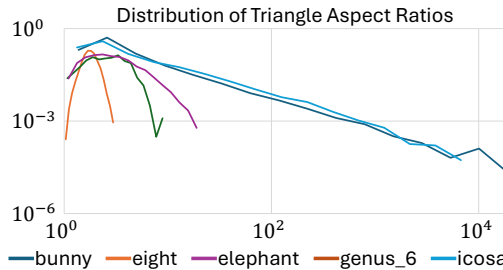


Figure 8: Distribution of triangle aspect ratios for the models visualized in Figure 6.

Lie Bracket

Comparison To evaluate our discretization of the Lie bracket, we compare to three approaches. The first two define the bracket indirectly, representing derivations in terms of functional maps [ABCCO13, AOCBC15]. The third is obtained analogously to ours, differentiating the finite-elements representation of Stein *et al.* [SWJG20] to obtain the covariant derivative and evaluating the expression $[X, Y](p) = \nabla Y|_p \cdot X(p) - \nabla X|_p \cdot Y(p)$. (For both finite-elements discretizations the obtained bracket $[X, Y]$ is not in the

Model	$\frac{\ \mathbf{M} - \mathbf{J}^\top \cdot \mathbf{M} \cdot \mathbf{J}\ _F}{\ \mathbf{M} + \mathbf{J}^\top \cdot \mathbf{M} \cdot \mathbf{J}\ _F}$	$\frac{\ \bar{\mathbf{T}} - \bar{\mathbf{J}}^\top \cdot \bar{\mathbf{T}} \cdot \mathbf{J}\ _F}{\ \bar{\mathbf{T}} + \bar{\mathbf{J}}^\top \cdot \bar{\mathbf{T}} \cdot \mathbf{J}\ _F}$	$\frac{\ \mathbf{T} - \mathbf{J}^\top \cdot \mathbf{A} \cdot \mathbf{J}\ _F}{\ \mathbf{T} + \mathbf{J}^\top \cdot \mathbf{A} \cdot \mathbf{J}\ _F}$
Bunny	1.5×10^{-16}	1.3×10^{-10}	1.0×10^{-10}
Eight	1.5×10^{-16}	2.2×10^{-16}	2.3×10^{-16}
Elephant	1.4×10^{-16}	1.6×10^{-15}	1.3×10^{-15}
Genus-6	1.4×10^{-16}	4.6×10^{-16}	3.7×10^{-16}
Icosa	1.4×10^{-16}	4.2×10^{-10}	3.1×10^{-10}

Table 2: Invariance under 90° -rotation, computed using the ratio of the Frobenius norm of the difference to the Frobenius norm of the sum.

span of the basis and we obtain the least-squares fit by solving the linear system in Equation 5 using the respective mass matrices. For our approach this requires approximating integrals using quadrature. For Stein *et al.*’s discretization, the bracket is piecewise linear, though not necessarily continuous across edge mid-points, and the integrals are computed in closed-form.)

We evaluate the discretizations of the Lie bracket on two tessellations of the sphere. For the first we recursively subdivide and refine the vertices of an icosahedron. For the second we randomly sample points on the sphere and compute the convex hull. Both tessellations contain approximately 10K vertices.

As input we use vector fields defined in the ambient 3D space. We start by generating random vector fields $\tilde{X}, \tilde{Y} : \mathbb{R}^3 \rightarrow \mathbb{R}^3$, whose Fourier coefficients are band-limited complex exponentials with uniformly randomly assigned Fourier coefficients. (Antipodal frequencies are assigned conjugate values so that the coordinate functions are real-valued.) Setting π to be the map projecting vector fields onto the tangent space of the unit sphere:

$$[\pi(Z)](p) \equiv Z(p) - p \cdot \langle Z(p), p \rangle,$$

we compute the projected vector fields $X = \pi(\tilde{X})$ and $Y = \pi(\tilde{Y})$, and obtain their Lie bracket as:

$$[X, Y] \equiv \pi(\nabla Y \cdot X - \nabla X \cdot Y).$$

Because \tilde{X} and \tilde{Y} are linear combinations of trigonometric functions, and because the projection π has a simple expression, the

	b	[ABCC013]	[AOCBC15]	[SWJG20]	Ours
icoso	2	3.5×10^{-3}	9.5×10^{-4}	1.0×10^{-4}	7.7×10^{-4}
	5	8.0×10^{-3}	1.5×10^{-3}	3.7×10^{-4}	2.4×10^{-3}
	10	2.6×10^{-2}	3.7×10^{-3}	7.3×10^{-4}	8.9×10^{-3}
	20	9.6×10^{-2}	1.1×10^{-1}	1.4×10^{-3}	3.5×10^{-2}
CH	2	1.7×10^{-1}	3.0×10^{-1}	9.6×10^{-3}	1.3×10^{-2}
	5	1.2×10^{-1}	3.1×10^{-1}	1.5×10^{-2}	1.6×10^{-2}
	10	1.3×10^{-1}	4.0×10^{-1}	2.2×10^{-2}	3.4×10^{-2}
	20	2.0×10^{-1}	4.6×10^{-1}	2.9×10^{-2}	9.6×10^{-2}

Table 3: Relative error in estimating the Lie bracket for of two vector fields for different band-widths, b , and different discretizations of the sphere, “icoso” vs. “CH”.

input vector fields X and Y , and the ground-truth bracket $[X, Y]$ can be evaluated in closed-form.

Table 3 gives the relative errors for the estimated bracket, computed for band-widths $b \in \{2, 5, 10, 20\}$, using the two tessellations of the sphere. (For the implementation of [AOCBC15] we computed the brackets using spectra of size varying from 10 to 1000 and give the smallest error across the different discretizations.)

As expected, the table shows that discretization accuracy deteriorates as vector-fields become higher frequency and as the tessellation becomes less uniform. In addition, we see that while all methods perform comparably on the subdivided icosahedron, the operator-based approaches are less robust in the case of non-uniform sampling. Interestingly, despite the continuity of their representation, we find that the finite-elements discretization of Stein *et al.* provides the best results. (In this case we use the same tessellations for all discretizations, so it is possible that some of the performance gain is due to the fact that Stein *et al.*’s basis has approximately $3 \times$ the numbers of degrees of freedom.)

Figure 9 visualizes the results, showing the bracket estimated using the four different approaches (first four columns) as well as the analytic solution (right), for vector fields \tilde{X} and \tilde{Y} with bandwidth $b = 10$. On the uniform tessellation of the sphere obtained by subdividing the icosahedron (top) all methods match the ground-truth. However, on the non-uniform tessellation the brackets computed using the operator-based approaches produce tangent vectors whose magnitudes do not match those of the ground-truth. (Note that visualizations are obtained by drawing vectors at triangle centers. Consequently, while the two visualizations in the rightmost column represent the same ground-truth vector field, they appear different because the vectors are drawn at different locations.)

Performance Under Refinement We also evaluate the performance of our method under refinement. To this end we construct tessellations of the torus by randomly sampling points in the periodic plane, computing the Delaunay triangulation, and mapping to the torus in 3D with inner (resp. outer) radius 2.0 (resp. 1.0):

$$\Phi(s, t) = (\cos(s), 0, \sin(s)) \cdot (2 + \cos(t)) + (0, \sin(t), 0).$$

As above, we synthesize band-limited vector-fields with uniformly random Fourier coefficients, $X, Y : \mathbb{R}^2 \rightarrow \mathbb{R}^2$, this time in the parameterization domain. Leveraging the metric-independence

of the Lie bracket, we obtain the ground-truth by analytically computing $[X, Y] : \mathbb{R}^2 \rightarrow \mathbb{R}^2$ and using the parameterization Φ to map it to 3D. We compare this to the bracket obtained by applying our method to the 3D vector fields obtained by applying Φ to X and Y .

Figure 10 (bottom left) shows the relative errors between the estimated and ground-truth brackets, computed for varying band-widths $b \in [1, 50]$ and averaged over ten different experiments. As expected, error increases with band-width and we find that error decreases consistently as we increase the resolution of the tessellation from $10K$ vertices to $160K$. The figure also shows an example of two vector-fields, X and Y , computed at a bandwidth of $b = 10$ using $40K$ vertices (top), and the estimated Lie bracket $[X, Y]$ (right), visualized using line integral convolution.

7. Conclusion and Future Directions

7.1. Properties

Choice of normals Our construction defines a discretization using the Phong interpolation of per-vertex normals. Implicit in this approach is the assumption that the interpolated normals are consistent with the triangle normal (e.g. they point in the same direction). For all our evaluations we defined per-vertex normals by summing the area-weighted normals of incident faces.

Rotation Like the discretizations of Knöppel *et al.* [KCPS13] and Stein *et al.* [SWJG20], assuming that the triangle mesh is orientable, our discretization is closed under the action of rotation by 90° (or any other fixed angle) in the tangent plane. In particular, this suggests that the discretization does not exhibit a preference for divergence-free vs. curl-free vector fields. This is in contrast, for example, to the Whitney 1-form basis that only exhibit curl in the interior of triangles, and whose 90° rotations are not contained in the space of Whitney 1-forms.

Relation to Scalar Gradients As with the discretization of Knöppel *et al.* [KCPS13], our vector-fields are continuous across the mesh. An implication of this is that they cannot represent the gradients of functions expressed in terms of the hat-basis, as those gradients are piecewise constant. However, it is straight-forward to incorporate the gradients of scalar functions within the vector-field-processing construction. (For example, one can integrate the gradients against the continuous basis vector-fields to get a “weak” representation that can then be used to find the projection onto the space of continuous vector fields by solving with the mass matrix.)

Implicit Geometry In our discretization, we implicitly treat the defined $\tilde{d}\Phi|_p$ operator as the differential of an embedding, using it to define the mapping from the tangent space of the unit right triangle to the tangent space of the sphere. However, there may not be any Φ whose differential is $\tilde{d}\Phi$. For example, the rows of $\tilde{d}\Phi|_p$ may not be curl-free. One immediate implication is that the associated second fundamental form, $\tilde{d}\Phi|_p^\top \cdot dN|_p$, need not be symmetric. In the future, we would like to explore addressing this limitation in one of two ways: (1) optimizing the per-vertex normals and (2) optimizing the definition of $\tilde{d}\Phi|_p$. Like the approach of Boubeker *et al.* [BA08], the latter approach could seek the geometry that fits the prescribed normals.



Figure 9: Visualization of the brackets computed for a frequency $b = 10$ function using a regular tessellation obtained by subdividing an icosahedron (top) and an irregular tessellation obtained by randomly sampling points on the unit sphere and computing the convex hull (bottom).

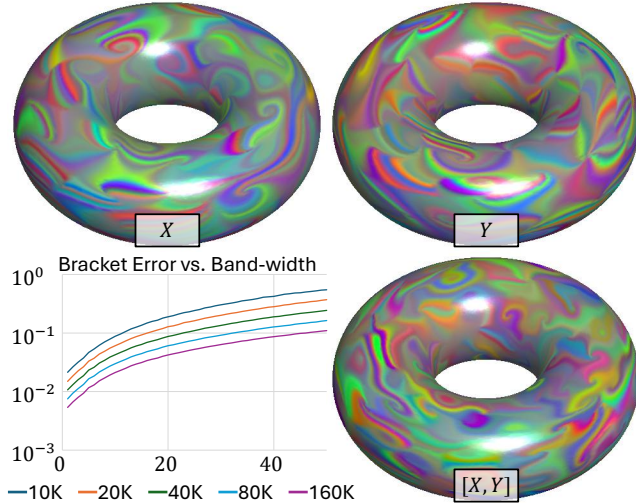


Figure 10: The relative error between the estimated Lie bracket of two vector fields on a torus and the analytic solution, given as a function of the band-width of the vector fields. The plots show that error increases with the frequency of the vector-fields, and decreases as the resolution is increased.

Acknowledgements

References

- [ABCC013] AZENCOT O., BEN-CHEN M., CHAZAL F., OVSJANIKOV M.: An operator approach to tangent vector field processing. *Computer Graphics Forum* 32, 5 (2013), 73–82. [9](#), [10](#)
- [AOCBC15] AZENCOT O., OVSJANIKOV M., CHAZAL F., BEN-CHEN M.: Discrete derivatives of vector fields on surfaces – an operator approach. *ACM Trans. Graph.* 34, 3 (May 2015). [9](#), [10](#)
- [BA08] BOUBEKEUR T., ALEXA M.: Phong tessellation. *ACM Trans. Graph.* 27, 5 (Dec. 2008). [2](#), [10](#)
- [CS13] CRANE K., SCHRÖDER P.: fieldgen. [7](#)
- [CWW17] CRANE K., WEISCHEDEL C., WARDETZKY M.: The heat method for distance computation. *Commun. ACM* 60, 11 (Oct. 2017), 90–99. [2](#)
- [dGLB*14] DE GOES F., LIU B., BUDNINSKIY M., TONG Y., DESBRUN M.: Discrete 2-tensor fields on triangulations. *Computer Graphics Forum* 33, 5 (2014), 13–24. [3](#)
- [DKT06] DESBRUN M., KANSO E., TONG Y.: Discrete differential forms for computational modeling. In *ACM SIGGRAPH 2006 Courses* (New York, NY, USA, 2006), SIGGRAPH '06, Association for Computing Machinery, p. 39–54. [2](#)
- [FSBS06] FISHER M., SPRINGBORN B., BOBENKO A. I., SCHRÖDER P.: An algorithm for the construction of intrinsic delaunay triangulations with applications to digital geometry processing. In *ACM SIGGRAPH 2006 Courses* (New York, NY, USA, 2006), SIGGRAPH '06, Association for Computing Machinery, p. 69–74. [7](#)
- [KCP13] KNÖPPEL F., CRANE K., PINKALL U., SCHRÖDER P.: Globally optimal direction fields. *ACM Trans. Graph.* 32, 4 (July 2013). [2](#), [5](#), [7](#), [10](#)
- [LC87] LORENSEN W. E., CLINE H. E.: Marching cubes: A high resolution 3d surface construction algorithm. In *Proceedings of the 14th Annual Conference on Computer Graphics and Interactive Techniques* (New York, NY, USA, 1987), SIGGRAPH '87, Association for Computing Machinery, p. 163–169. [8](#)
- [Loo87] LOOP C.: *Smooth Subdivision Surfaces Based on Triangles*. Master's thesis, January 1987. [6](#), [8](#)
- [PFS*19] PARK J. J., FLORENCE P., STRAUB J., NEWCOMBE R., LOVEGROVE S.: DeepSDF: Learning continuous signed distance functions for shape representation. In *Conference on Computer Vision and Pattern Recognition (CVPR)* (2019), pp. 165–174. [5](#)
- [SC*19] SHARP N., CRANE K., ET AL.: Geometrycentral: A modern c++ library of data structures and algorithms for geometry processing. [7](#)
- [SSC19] SHARP N., SOLIMAN Y., CRANE K.: The vector heat method. *ACM Trans. Graph.* 38, 3 (2019). [5](#), [6](#), [7](#)
- [SWJG20] STEIN O., WARDETZKY M., JACOBSON A., GRINSPUN E.:

A simple discretization of the vector dirichlet energy. *Computer Graphics Forum* 39, 5 (2020), 81–92. [5](#), [7](#), [9](#), [10](#)

[Tay08] TAYLOR M. A.: Asymmetric cubature formulas for polynomial integration in the triangle and square. *J. Comput. Appl. Math.* 218, 1 (Aug. 2008), 184–191. [4](#)

Appendix A: Bracket Comparison

As noted by Stein *et al.*, since their expression of the covariant derivative that can be evaluated point-wise, one can use the factorization of endomorphisms (Section 3.1) to define a Killing energy.

Figure 11 compares the smallest eigenvectors obtained using our discretization of the Killing energy (first row), with the eigenvectors obtained using Stein *et al.*’s discretization. As noted in that work, directly using the Killing energy defined by their discretization is not robust due to spurious minimizers. They address this by adding an additional total connection energy to their Killing energy. The different rows show the eigenvectors obtained using Stein *et al.*’s discretization for progressively larger values of α . Vector fields are visualized using small arrows, overlaid on flow-line visualizations generated using line integral convolution. The image also shows the associated eigenvalue in the top left corner of each figure.

While a small regularization weight $\alpha = 10^{-4}$ effectively generates the as Killing-as-possible vector-field associated with the near rotational symmetry of the pulley, the problem with spurious minima is evident in the subsequent eigenvectors. This is mitigated by increasing the smoothness to $\alpha = 10^{-3}$, though even in this case one sees artifacts in the right-most column. Further increasing the regularization weight to $\alpha = 10^{-2}$ produces results visually similar to ours, and with similar eigenvalues. Further increasing the regularization weight can have the detrimental effect of biasing the spectral decomposition away from Killing vector fields in preferences of vector-fields that are smoother.

This highlights a limitation observed by Stein *et al.*— While their basis provides desirable properties desirable for the connection Laplacian (e.g. linear reproduction), the underlying Crouzeix-Raviart basis is discontinuous and can result in artifacts when used to define other energies.

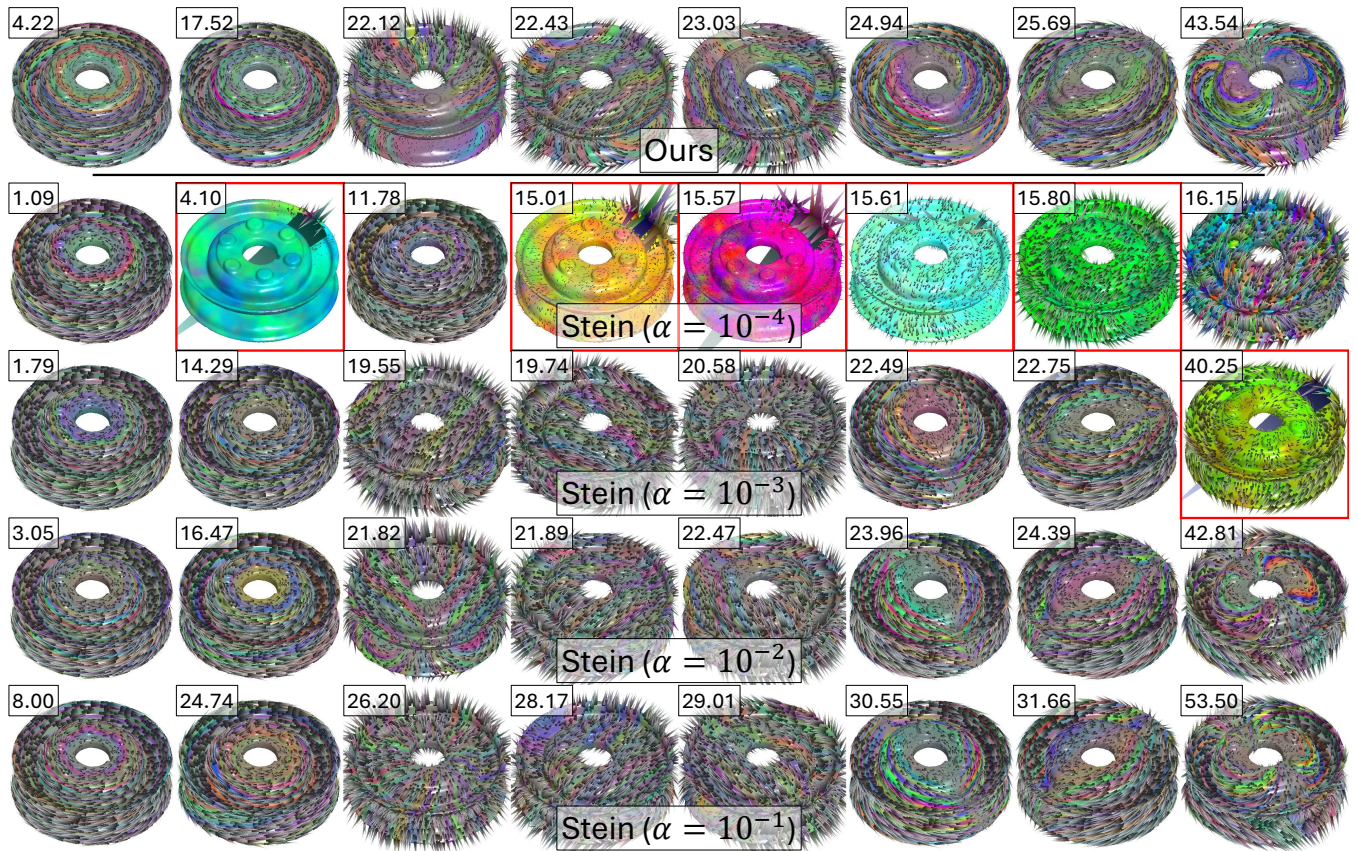


Figure 11: Spectra of the Killing energy: Comparing the smallest eigenvectors obtained using our approach (top row) with the smallest eigenvectors obtained Stein et al.'s method (second through fifth rows), with different regularization weights α . Spurious minima are highlighted in red.